Intermetallics 160 (2023) 107946

Contents lists available at ScienceDirect

Intermetallics

journal homepage: www.elsevier.com/locate/intermet

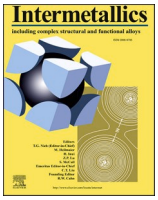

Critical influence of phase transition on the hydrogen evolution reaction activity of Heusler alloys

Zuwei Fan [a,b], Peng Zou [b], Kemin Jiang [b], Wei Xu [b], Meng Gao [b], Vladislav Zadorozhnyy [c], Guowei Li [b,**], Juntao Huo [b,*], Jun-Qiang Wang [b,***]

[a] School of Materials Science and Chemical Engineering Ningbo University, Ningbo, 315211, China
[b] CAS Key Laboratory of Magnetic Materials and Devices and Zhejiang Province Key Laboratory of Magnetic Materials and Application Technology, Ningbo Institute of Materials Technology and Engineering, Chinese Academy of Sciences, Ningbo, 315201, China
[c] National University of Science and Technology MISIS, Leninsky Prosp. 4, 119049, Moscow, Russia

ARTICLE INFO

Keywords:
Heusler alloy
Phase transition
Austenite phase
Martensite phase
Hydrogen evolution reaction
Electrocatalyst

ABSTRACT

Unraveling structure-property relationships is of critical importance for designing superior catalysts. Heusler alloys are a family of materials whose atomic packing structure may change with a change in the external field, for example, temperature, magnetic field, and/or stress, and are ideal models for studying the structure-property relationship. In this study, a series of Ni–Mn–Sn–Co Heusler alloys with controlled phases and compositions, including the tetragonal martensite phase ($Ni_{46}Mn_{36}Sn_{11}Co_7$, labeled Co7), cubic austenite phase ($Ni_{42}Mn_{43}Sn_{10}Co_5$, labeled Co5), and tetragonal/cubic mixing phase ($Ni_{46}Mn_{38}Sn_{12}Co_4$, labeled Co4) were investigated. The alloys with the martensitic phase exhibited superior catalytic activity toward hydrogen evolution reaction (HER) than those with the austenitic phase. At an overpotential of 350 mV, the HER current density of the martensite phase of the Co7 sample was almost 2 times higher than that of the austenite phase of the Co5 sample. In-situ temperature-dependent catalytic measurements for the Co4 alloy suggest that the catalytic activity decreases significantly when phase transformation from martensite to austenite occurs. The efficient electron transfer kinetics and low electron work function are responsible for the high activity of the martensite phase, according to Tafel and work function analyses. These results provide a promising strategy for the development of high-performance Heusler alloys by controlling their phase structures and phase transitions.

1. Introduction

Amid the current energy crisis and environmental issues, hydrogen is believed to be a promising alternative to traditional fossil fuels [1,2]. Catalysts play a significant role in reducing overpotentials and energy consumption in highly efficient and low-cost hydrogen production processes. Therefore, the development of an electrocatalyst material with high activity, high stability, and low cost is a prerequisite for applying the electrocatalytic water decomposition method to produce hydrogen [3]. Generally, there are two strategies for improving the efficiency of a catalyst. One is to maximize the number of catalytically active sites, which can boost the apparent efficiencies at fixed working potentials. This can be achieved using strategies such as nanostructuring [4–7], single atom design [8,9], or highly efficient precious metal loading [10–13]. Another method is to optimize the catalytically active sites to achieve higher intrinsic activities. Typical methods include electronic structure tailing via elemental doping, formation of heterojunction, and high-entropy intermetallic compounds [14,15], in addition, topological semimetals, such as Weyl semimetals, Dirac semimetals, and nodal line semimetals, are also potential and efficient catalysts [16]. and introduction of external stimuli [17,18].

Notably, the use of phase transition engineering for designing high-performance catalysts has received increasing attention. Yang et al. found that a Pd–Cu alloy with a *bcc* phase could be regarded as a highly active electrocatalyst for hydroxide oxidation in alkaline electrolytes [19]. Wang et al. used nickel to evaluate the role of the crystal structure of an electrocatalyst in the analysis of oxygen [20]. Currently, studies on the phase structure to regulate the catalytic performance of hydrogen

* Corresponding author.
** Corresponding author.
*** Corresponding author.
E-mail addresses: liguowei@nimte.ac.cn (G. Li), huojuntao@nimte.ac.cn (J. Huo), jqwang@nimte.ac.cn (J.-Q. Wang).

https://doi.org/10.1016/j.intermet.2023.107946
Received 2 March 2023; Received in revised form 4 May 2023; Accepted 8 May 2023
Available online 13 May 2023

evolution mainly focus on element doping and the annealing process [21–23]. However, element doping changes the catalyst composition and introduces uncertainties in understanding the working mechanisms. To date, the influence of phase structure on catalytic processes remains an open question. Recently, Co-based Heusler alloys have been proposed as promising catalysts for energy conversion [24–27] owing to their tunable elemental composition and low cost [28]. However, the hydrogen evolution reaction (HER) efficiencies of most Heusler compounds cannot fulfill the requirements of industrial-scale hydrogen production [29]. By changing the compositions and elemental combinations, hundreds of compounds with tunable electronic and crystal structures can be obtained. More importantly, their phase structures and phase transition behaviors can be precisely designed [30–32]. This provides an ideal platform for investigating the influence of phase structures and limitations of their catalytic activities.

In this study, Co-based Heusler alloys with the desired phase structures were synthesized by carefully tailoring the compositions. By carefully assessing the intrinsic HER activities of the pure austenite (A) and martensite (M) phases, and their mixtures (A + M), we found that the M phase was the best choice. To reveal the influence of the phase structures, a Heusler compound with a first-order phase change at room temperature was designed [33–35]. Notably, the HER activities significantly decreased on transition from the low-temperature M phase to the high-temperature A phase. Using a combination of Tafel and ultraviolet photoelectron spectroscopy (UPS) analyses, it was confirmed that the M phase has a lower electron transfer resistance and is more powerful in maintaining the *d*-band centers that favor the hydrogen evolution process. Our findings highlight the importance of phase control in the search for and design of high-performance alloy catalysts with multiple phases.

2. Experimental details

2.1. Sample preparation

Three Ni–Co–Mn–Sn alloy ribbons with different compositions were fabricated by the arc melting method with the corresponding high-purity elements (>99.9 wt %). The melting loss rate of the as-cast alloys was <1%. To avoid the occurrence of a large amount of second-phase precipitation, the copper roller rapid quenching method was used to prepare the ribbons. Ribbons with lengths of 10–40 mm, widths of 1–2 mm, and thicknesses of 60–70 μm were obtained at a linear speed of 10 m/s. This type of self-supporting ribbon also facilitates subsequent experimental research on the catalysis of electrochemical hydrogen evolution. Three as-spun ribbon samples were prepared: $Ni_{46}Mn_{36}Sn_{11}Co_7$, $Ni_{42}Mn_{43}Sn_{10}Co_5$, and $Ni_{46}Mn_{38}Sn_{12}Co_4$ (at. %).

2.2. Material characterization

The phase constitution and microstructures of the samples were examined by X-ray diffraction (XRD, Bruker D8 Advance, Germany) using Cu Kα radiation, field emission scanning electron microscopy (FE-SEM, Quanta 250, FEI, USA), and transmission electron microscopy (TEM, Talos F200×, ThemoFisher, USA). The TEM samples were prepared using an ion beam thinner (Gatan 691, Gatan, USA). Furthermore, in-situ XRD was performed to characterize the change in the phase structure of the ribbons during the heating process. Differential scanning calorimetry (DSC 214) was used determine the phase transition temperatures of the alloys. The phase transition temperatures were calibrated, and suitable ribbons were subjected to in-situ water splitting electrocatalysis experiments. The work functions and Fermi energy level positions of the materials were measured by ultraviolet photoelectron spectroscopy (UPS, Axis Ultra DLD).

2.3. Electrochemical measurements

Electrochemical measurements were performed at different temperatures using an electrochemical workstation (Zahner Zennium) with a three-electrode configuration. A platinum sheet was used as the counter electrode, an Ag/AgCl electrode with 3.5 M KCl was selected as the reference electrode, and Ni–Mn–Co–Sn alloy ribbons were used as the working electrode (WE). All tests were performed in a 1 M KOH solution.

In the linear sweep voltammetry (LSV) measurement, the voltage applied to the WE was swept linearly from +0.1 V to −0.6 V vs. the reversible hydrogen electrode (RHE) at a scan rate of 5 mV/s. The relevant RHE potential was calculated using the Nernst equation [$E_{(RHE)} = E_{(Ag/AgCl)} + E$ (standard electrode potential) + 0.059 × pH], where E (standard electrode potential) $= -7.37 * 10^{-4} * T + 0.2268$ (T is the work temperature).

The chronoamperometry (*j*-t) test is as follows: Under an overpotential of −1.4 V, the current density was stabilized and then heated, and the temperature was recorded every minute.

The frequency range of the electrochemical impedance spectroscopy (EIS) test was $0.1-10^5$ Hz, and the potential was −1.45 V (vs. RHE). An equivalent circuit simulator was used to obtain the solution resistance (R_s) and charge transfer resistance (R_{ct}). The equivalent electrical circuit model of R (QR) was used to fit the EIS data using the ZSimpWin 3.50 software.

The electrochemically active surface area (ECSA) was estimated from the electrochemical double-layer capacitance of the hybrids, which was determined from the cyclic voltammetry (CV) curves measured in the potential range close to the open-circuit potential (±50 mV vs. RHE).

For the in situ warming experiments, a constant-temperature water bath was used and the temperature in the electrolytic cell was measured using a thermocouple probe, and the temperature difference was controlled at 1 K.

3. Results and discussion

3.1. Crystal and phase structures of Heusler alloys

The $L2_1$ austenite structure of the Ni–Co–Mn–Sn Heusler alloys is shown in Fig. 1(a) The Sn and Mn atoms occupy the 4*a* (0, 0, 0) and 4*b* (0.50, 0.50, 0.50) positions, respectively, and Ni (Co) atoms occupy the 8*c* (0.25, 0.25, 0.25) and (0.75, 0.75, 0.75)) positions. It has been reported that the valence electron concentration (e/a) can be used to tailor the phase transformation temperature and phase structures [36,37] thus, we changed the number of valence electrons by tailoring the Co content. The pure austenite (A) and martensite (M) phases, and their mixtures (A + M) can thus be obtained.

In the material synthesis process, rapid solidification technology is employed to eliminate the existence of a second phase in the parental alloys [38,39] (Fig. 1 (b)). This is because the single roller rapid solidification ribbon throwing technology can enable the cooling rate of the high-temperature melt to attain a value greater than 10^6 K/s and rapidly solidified ribbons in a single-phase form can be obtained with a highly uniform composition; three ribbons with different Co atomic ratios were synthesized accordingly: $Ni_{46}Mn_{36}Sn_{11}Co_7$ (labeled Co7), $Ni_{42}Mn_{43}Sn_{10}Co_5$ (labeled Co5), and $Ni_{46}Mn_{38}Sn_{12}Co_4$ (labeled Co4). Fig. 1(c) shows the corresponding XRD patterns of the as-prepared samples at room temperature. Co5 crystallized in the $L2_1$ *fcc* structure with typical (220) reflections, which can be attributed to the pure austenitic phase, as reported in a previous work [40]. In contrast, the Co7 sample crystallized into an orthorhombic martensitic structure with the (125) reflection, suggesting the existence of martensite [41]. Notably, a mixture of martensite and retained austenite was observed in the Co4 sample at room temperature. Thus, changes in the catalytic activity during the phase transition from the martensite to austenite can be monitored. The high quality of the as-prepared ribbons was further

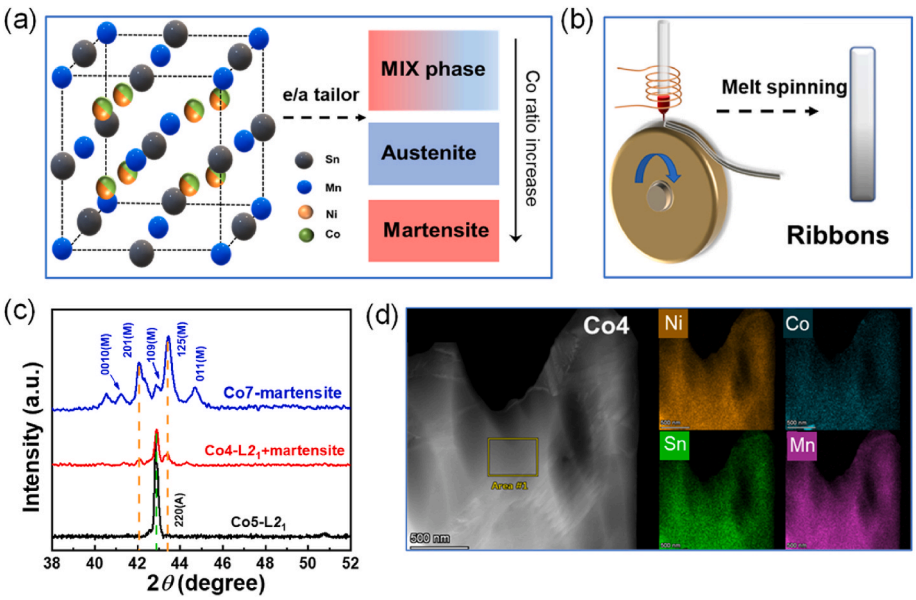

Fig. 1. (a) Crystal structures of the Ni–Co–Mn–Sn Heusler alloys and their phase structure control strategy. (b) Process of composition modulation of the Ni–Mn–Sn–Co ribbons and the process of ribbon preparation. (c) XRD patterns of the Heusler alloy ribbons with different compositions and phases. (d) HAADF image and EDS elemental mapping of the Co4 sample.

confirmed by high-angle annular dark field (HAADF) imaging and energy-dispersive X-ray spectroscopy (EDS) (Fig. 1(d), Fig. S1), where a uniform elemental distribution was observed for all samples.

The differences in the phase structures were further confirmed by TEM. Fig. 2a shows the low-magnification TEM bright-field image of Co4 with flaky martensitic variants distributed along the grain boundaries. Three satellite points (marked by red arrows) representing the typical diffraction properties of the modulated 4*O* structures can be observed in the inset of Fig. 2(a), which shows the selected area electron diffraction (SAED) pattern of Co4. This indicates the coexistence of the martensite and austenite phases at room temperature, which agrees with the result of XRD. Only the austenite phase was observed in the Co5 sample, as shown in Fig. 2(b), which could be confirmed as a symmetrical L2_1 structure from its corresponding SAED pattern (inset). The bright-field TEM image of the 10 M version of strip martensite in Co7 is shown in Fig. 2(c), and the corresponding SAED pattern shows four satellite points between the fundamental maxima. These results confirm that the three components have different phase structures at room temperature.

To investigate the catalytic behavior at room temperature and subsequent temperature-dependent activity changes, it is important to determine the phase transition temperatures of the ribbons. The DSC

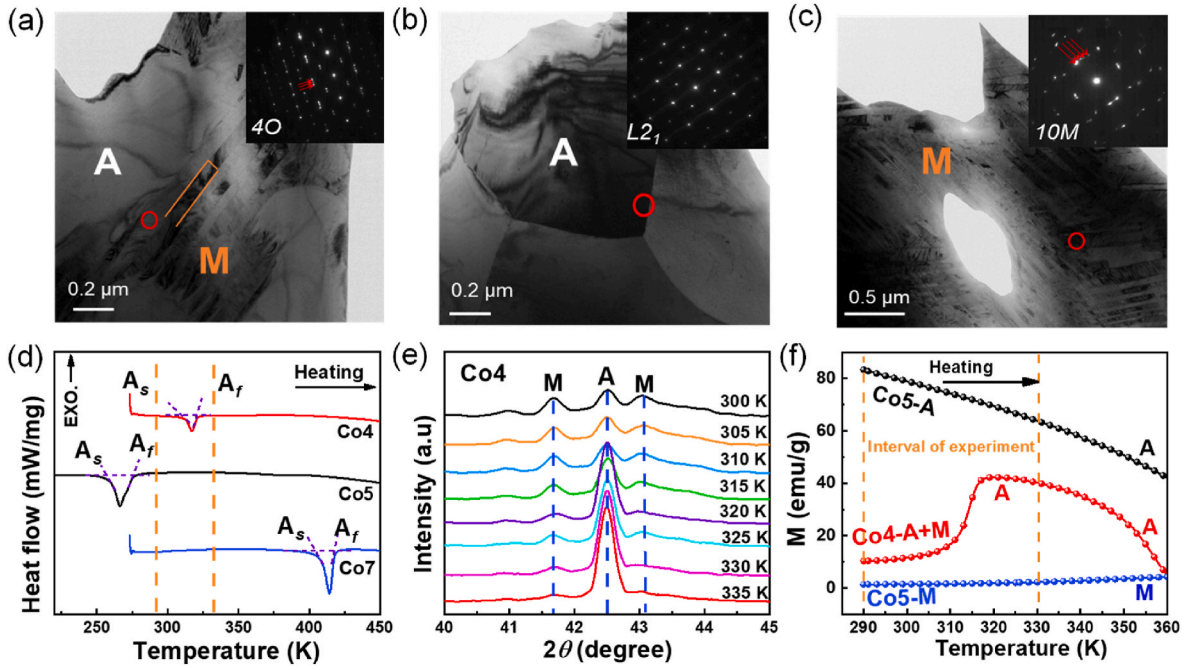

Fig. 2. Confirmation of phase transition. (a)–(c) TEM images of the ribbons alloy with different compositions at room temperature. Low magnification TEM bright field images and the corresponding SAED patterns (insets) of Co4, Co5, and Co7, respectively. (d) DSC curves of the alloys with different compositions. (e) Variable-temperature XRD patterns of Co4. (f) M-T curves of the electrode materials with different compositions.

curves during the heating process are shown in Fig. 2(d), where A_s is the start temperature of the martensite to austenite phase transition and A_f is the end temperature. As shown in the figure, the A_s of Co5 is approximately 260 K, while that of Co7 and Co4 is approximately 407 K and 311 K, respectively. These phase change behaviors were further confirmed by in situ variable-temperature XRD experiments, as shown in Fig. 2(e). For the Co4 sample, the peaks corresponding to the martensite phase decreased gradually with increasing temperature. In contrast, the characteristic (220) peak of the cubic austenite phase became the main peak after the phase transition. The position and shape of the peaks were almost unchanged for the Co5 and Co7 samples without any phase transition (Fig. S2), which provided a control group for subsequent electrochemical experiments. As another strong evidence for the phase transition, magnetic measurements (as a function of temperature) show that only the Co4 alloy ribbons exhibit magnetic mutations during the phase transformation process (Fig. 2(f)). The results of in situ heating SEM, shown in Fig. S3(a)–(f), show the phase transition process more precisely. Evidently, the Co4 alloy exhibited a mixed phase of martensite and austenite at room temperature, and the martensite gradually disappeared with an increase in temperature until it completely became the austenitic phase. The results suggest that the Co7, Co5, and Co4 samples crystallized in martensitic, austenite, and mixed phases during the catalytic measurements at room temperature. Notably, the phase transition of the Co4 ribbon was completed slightly above room temperature, thereby enabling the investigation of the influence of the phase transition using the water-bath heating technique.

3.2. Electrochemical measurements

The electrochemical HER performances of the three samples with different phase structures were assessed by LSV, wherein the curves were either normalized by the geometric areas or electrochemical surface areas (ECSAs) [42]. The Co7 catalyst with a pure martensitic phase exhibited the best HER activity with a current density of 10 mA cm^{-2} at an overpotential of 290 mV (Fig. S4). It exhibits a good catalytic activity in numerous pristine Ni–Co alloys, as shown in Table S1. The intrinsic activities were obtained by measuring the corresponding ECSAs (Fig. S5) and normalizing the activity area, as shown in Fig. 3(a), (the detailed calculation process is provided in the Supplementary Information) [43,44]. The Co7 catalyst with the martensitic phase exhibited the best intrinsic catalytic activity. At a given overpotential of −0.3 V, the current density of the Co7 martensite phase was 0.063 mA cm^{-2}, which is twice that of the Co5 austenite phase (0.035 mA cm^{-2}) The Tafel slopes of the catalysts were calculated from the LSV curves. As shown in Fig. 3 (b), Co7 shows a smaller Tafel slope (118 mV dec^{-1}) than those of the Co5 (140 mV dec^{-1}) and Co4 (120 mV dec^{-1}) catalysts. The Tafel slope indicates that the kinetic process of the alloy ribbon is dominated by either the Volmer or Heyrovsky rate-determining step, with high hydrogen coverage [45,46].

To investigate the role of phase structures on catalytic behavior, we conducted an in-situ thermal phase change analysis of hydrogen evolution by water electrolysis. The current density vs. temperature curves for each catalyst were recorded at a constant voltage of −1.4 V vs. Ag/AgCl (Fig. 3(c)). A continuous increase was observed for all three investigated samples. This is not unusual, as the increase in temperature increases the rate constant according to the Arrhenius law. However, in comparison with the Co7 and Co5 samples, which exhibited no phase transitions, the temperature-dependent activities of the Co4 sample deviated from the rate constant-dominated model in the temperature range of the phase transition. To exclude experimental errors during the heating process, the relationship between the heating time and temperature was studied (as shown in Fig. S6). Evidently, the heating rates of the three electrodes during the heating process were basically the same, indicating that other factors must be affecting the activity enhancement in addition to the well-known temperature activity enhancement.

Fig. 3(d) shows the LSV curves of the Co4 sample at different temperatures. The overpotential decreased at elevated temperatures. In contrast to the linearly increasing overpotentials exhibited by the Co5 and Co7 samples, the overpotential for the Co4 sample at a current density of 10 mA cm^{-2}, decreased linearly before the phase transition and deviated from the linear relationship after the phase transition (Fig. 3(e), Fig. S7). The slope becomes significantly smaller, indicating that it is possible that the austenite phase structure becomes more after

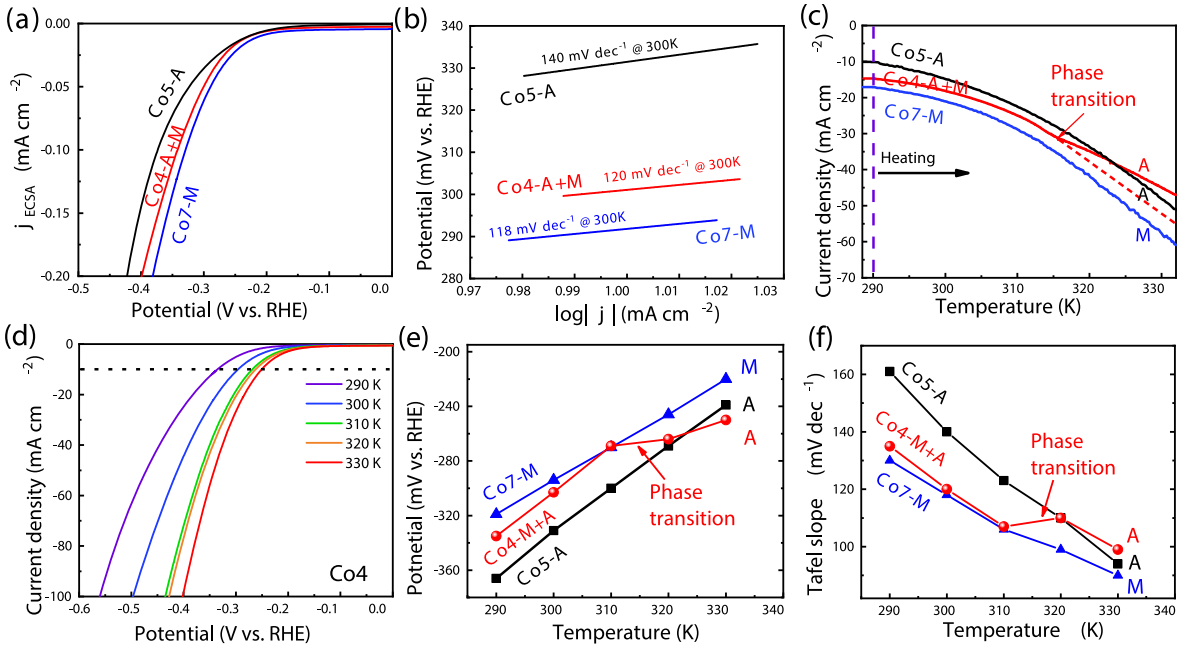

Fig. 3. Measurement of the electrocatalytic activity. (a) ECSA-normalized LSV curves of the catalysts in 1 M KOH solution. (b) Tafel slopes of the different electrodes at room temperature. (c) Current density curves as a function of temperature for each electrode at a constant voltage. (d) LSV curves of the Co4 alloy ribbons at different temperatures. (e) Dependence of overpotential on temperature for the different electrodes at 10 mA cm^{-2}. (f) Dependence of the Tafel slopes on temperature for the materials exhibiting a phase change and those with no phase change.

the phase transformation, which hinders the further promotion of HER catalysis by temperature. The Tafel slopes decreased with increasing temperature (Fig. 3(f)and S8). However, the Tafel slope of the Co4 sample increased to a higher value at the phase change temperature (~320 K), this strengthens the plausibility of our speculation in the previous text that the increase of the austenite phase hinders the HER catalytic process.

To understand the underlying reason for the phase change-induced activity deterioration, EIS data were measured at different temperatures, as shown in Fig. S9. A Randles circuit including the solution resistance (R_s), charge transfer resistance (R_{ct}), and equivalent capacitance (CPE) was used to fit the results. The R_{ct} of the Co5 and Co7 samples decreased with increasing temperature, whereas that of Co4 increased from 2.6 to 2.9 Ω in the phase transition temperature zone, which undoubtedly hindered the electrolytic water splitting process (Fig. 4(a)). Notably, the R_s values of each component alloy catalyst showed only marginal differences at different temperatures, as shown in Fig. S7(d), and decreased linearly with increasing temperature for all catalysts. The control experiment showed that the influence of temperature can be excluded.

According to Sabatier's principle, the free energy of hydrogen adsorption (ΔG_H), which is based on the *d*-band centers, plays a decisive role in understanding HER activities [47–50]. However, it is difficult to obtain the variation of hydrogen adsorption energy directly due to the large size of the four-atom crystals. The change in the work function and Fermi energy level of the material also significantly affects the catalytic performance of the material [51–54]. Therefore, an effort was made from these two aspects to explain why the Heusler alloys in the martensitic phase exhibit a better HER catalytic potential. The work function of the electrode material and position of the Fermi level can be obtained from UPS analysis [55]. The magnitude of the work function and the position of the Fermi level can be calculated using Equations (1) and (2):

$$W_f = h\nu - E_{\text{cutoff}} \tag{1}$$

$$E_{\text{Fermi level}} = 0 - W_f \tag{2}$$

where W_f is the work function, $h\nu$ is the energy of the excitation light source He I (21.2 eV), E_{cutoff} is the secondary electron cutoff energy of the material, and $E_{Fermi\ level}$ is the Fermi level position.

The UPS test results for the three samples are shown in Fig. 4(b)–(d). From the figures that as the temperature increases, the secondary electron cutoff energy of all samples shifts to the left, with the specific values in Fig. S10, and the values of the work function for all samples are calculated in conjunction with Eq. (1) in Fig. 4(e)–(g). The work function of all samples decreases with increasing temperature, which is due to the accelerated electron motion promoted by temperature. With an increase in the temperature from 298 to 335 K (which is after the phase transition temperature), the work function of the Co4 ribbons decreased

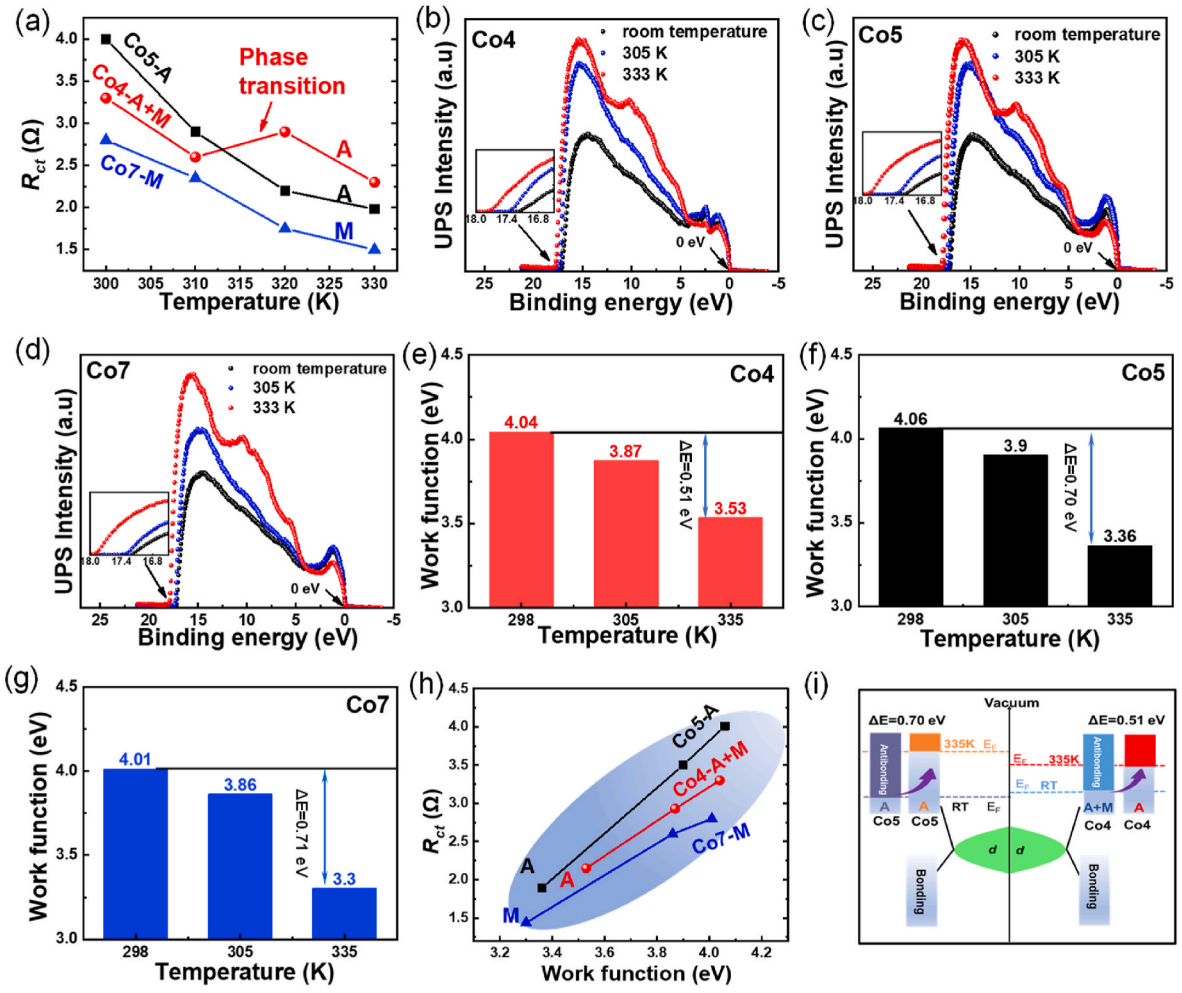

Fig. 4. Analysis of the catalytic mechanism of different electrode materials. (a) Variation curve of the charge transfer resistance (R_{ct}) with temperature. (b)–(d) In-situ ramp-up UPS analysis curves of Co4, Co5 and Co7 electrode materials, respectively. (e)–(g) Histogram of the work functions of Co4, Co5 and Co7 electrode materials at different temperatures, respectively. (h) R_{ct} vs. work function, which exhibits a positive relationship for all the materials. (i) Changes in the Fermi energy level during phase transition of the Co electrode material.

from 4.04 to 3.53 eV. This differential value (0.51 eV) is significantly smaller than those for the Co5 (0.70 eV) and Co7 samples (0.71 eV) without any phase transition. This indicates that the increase of the austenite phase reduces the decrease of the work function, making it difficult for electrons to escape to the electrode surface, thus inhibiting the HER process.

Combined with the R_{ct} variation in the previous section, we further to understand how the austenitic phase hinders the HER process. As shown in Fig. 4(h). R_{ct} is positively correlated with the work function, that is, a smaller work function facilitates charge transfer. At the same temperature, the martensite phase exhibited a lower R_{ct} and work function than the austenite phase. Upon heating, both R_{ct} and the work function decreased for all three samples. The reduction in impedance and work function during the heating process for the Co4 material exhibiting a phase transition was considerably smaller than that for the Co5 and Co7 materials without any phase transition; that is, the austenite phase hinders the charge transfer process.

With the changes in the work function, the influence of phase transition on the HER activities can be understood by tailoring the Fermi level. As shown in Fig. 4(i), the shift of the Fermi level influences the position of *d*-band centers and thus controls the electron filling of the antibonding states. The filling of the antibonding orbitals is closely related to the adsorption energy of hydrogen and HER kinetics [56,57].

Evidently, the decrease in the percentage of antibonding orbitals after the phase transition of Co4 is small. In contrast, compared to other samples without phase transition (e.g., Co5), the Fermi energy level rises more away from the *d*-band center during the warming process. It is reasonable to assume that the austenitic phase in the alloy increases and the martensitic phase decreases due to the phase transformation of the Heusler alloy. This affects the movement of the Fermi energy level and thus the occupation of electron orbitals in the alloy. Specifically, the martensite phase occupies more bonding orbitals than the austenite phase in the HER process, indicating that the binding energy of hydrogen intermediates on the electrode surface and the electrolytic water splitting process in an alkaline environment is higher for the pure martensite phase than that for the austenite phase. Water is more easily dissociated to obtain hydrogen precipitation intermediates, accelerating the electrochemical adsorption process and resulting in higher catalytic activity [58–61]. Considering that the high Tafel slopes are a result of the high hydrogen coverage and low charge transfer coefficient of the Heusler catalysts, we can conclude that the martensite phase Heusler alloy with lower electron transfer resistance and faster electrochemical adsorption process is preferred for HER catalysis.

4. Conclusion

Heusler alloys with controlled phase structures and phase-transition behaviors were synthesized. The phase-structure-dependent HER activities, as well as the influence of phase transitions, were investigated by carefully controlling the alloy composition and transition temperature. The experimental results show that the martensitic phase structures of these alloys exhibit superior catalytic activity, which can be attributed to the lower work function for the electron transfer. This study provides a guide for the use of Heusler alloys with controlled phase structures as potential catalysts.

Credit author statement

Zuwei Fan: Data curation, Writing – original draft. **Peng Zou:** Data curation, Writing – original draft. **Kemin Jiang:** Conceptualization, Methodology, Writing – review & editing. **Wei Xu:** Conceptualization, Methodology, Writing – review & editing. **Meng Gao:** Conceptualization, Methodology, Writing – review & editing. **Vladislav Zadorozhnyyc:** Conceptualization, Methodology, Writing – review & editing. **Guowei Li:** Conceptualization, Methodology, Writing – review & editing. **Juntao Huo:** Conceptualization, Methodology, Writing – review & editing. **Jun-Qiang Wang:** Conceptualization, Methodology, Writing – review & editing.

All authors listed have made a significant contribution to the research reported and have read and approved the submitted manuscript, and furthermore, all those who made substantive contributions to this work have been included in the author list.

Declaration of competing interest

The authors declare that they have no known competing financial interests or personal relationships that could have appeared to influence the work reported in this paper.

Data availability

Data will be made available on request.

Acknowledgment

The authors acknowledge the financial supports from the National Key R&D Program of China (2018YFA0703600), National Natural Science Foundation of China (NSFC 52222105, 51827801, 52071327, 92163108, 52271194), Youth Innovation Promotion Association CAS (No. 2019296), Ningbo Yongjiang Talent Introduction Programme (2022A-090-G), the Hundred Talents Programs in Chinese Academy of Science, the Foundation of Director of NIMTE, and Zhejiang Provincial Natural Science Foundation of China (LR22E010004, 2022C01023). Prof V. Zadorozhnyy also acknowledges the support from the Federal Academic Leadership Program Priority 2030 (K1-2022-032).

Appendix A. Supplementary data

Supplementary data to this article can be found online at https://doi.org/10.1016/j.intermet.2023.107946.

References

[1] H.L. van Soest, M.G.J. den Elzen, D.P. van Vuuren, Net-zero emission targets for major emitting countries consistent with the Paris Agreement, Nat. Commun. 12 (1) (2021) 2140, https://doi.org/10.1038/s41467-021-22294-x.
[2] D. Zhang, J. Wang, Y. Lin, Y. Si, C. Huang, J. Yang, B. Huang, W. Li, Present situation and future prospect of renewable energy in China, Renew. Sustain. Energy Rev. 76 (2017) 865–871, https://doi.org/10.1016/j.rser.2017.03.023.
[3] S. Wang, A. Lu, C.J. Zhong, Hydrogen production from water electrolysis: role of catalysts, Nano. Converg. 8 (1) (2021) 231–254, https://doi.org/10.1186/s40580-021-00254-x.
[4] X. Xiong, Z. Cai, D. Zhou, G. Zhang, Q. Zhang, Y. Jia, X. Duan, Q. Xie, S. Lai, T. Xie, Y. Li, X. Sun, X. Duan, A highly-efficient oxygen evolution electrode based on defective nickel-iron layered double hydroxide, Sci. China Mater. 61 (7) (2018) 939–947, https://doi.org/10.1007/s40843-017-9214-9.
[5] Y. Sun, T. Zhang, X. Li, Y. Bai, X. Lyu, G. Liu, W. Cai, Y. Li, Bifunctional hybrid Ni/Ni2 P nanoparticles encapsulated by graphitic carbon supported with N, S modified 3D carbon framework for highly efficient overall water splitting, Adv. Mater. Interfac. 5 (15) (2018), 1800473, https://doi.org/10.1002/admi.201800473.
[6] X.Z. Liu, S. Ju, P. Zou, L.J. Song, W. Xu, J.T. Huo, J. Yi, G. Wang, J.Q. Wang, Advanced catalyst for hydrogen evolution reaction by dealloying Al-based nanocrystalline alloys, J. Alloys Compd. 880 (2021), 160548, https://doi.org/10.1016/j.jallcom.2021.160548.
[7] Q. Sang, S. Hao, J. Han, Y. Ding, Dealloyed nanoporous materials for electrochemical energy conversion and storage, Energy 4 (1) (2022), 100069, https://doi.org/10.1016/j.enchem.2022.100069.
[8] Y. Wang, Y. Zhang, W. Yu, F. Chen, T. Ma, H. Huang, Single-atom catalysts for energy conversion, J. Mater. Chem. 2050 (2023) 7488–7496, https://doi.org/10.1039/d2ta09024d.
[9] J. He, J. Liu, Y. Hou, Y. Wang, S. Yang, H.G. Yang, Surface chelation of cesium halide perovskite by dithiocarbamate for efficient and stable solar cells, Nat. Commun. 11 (1) (2020) 4237, https://doi.org/10.1038/s41467-020-18015-5.
[10] L. Xie, Q. Liu, X. Shi, A.M. Asiri, Y. Luo, X. Sun, Superior alkaline hydrogen evolution electrocatalysis enabled by an ultrafine PtNi nanoparticle-decorated Ni nanoarray with ultralow Pt loading, Inorg. Chem. Front. 5 (6) (2018) 1365–1369, https://doi.org/10.1039/c8qi00120k.
[11] D. Hou, W. Zhou, X. Liu, K. Zhou, J. Xie, G. Li, S. Chen, Pt nanoparticles/MoS2 nanosheets/carbon fibers as efficient catalyst for the hydrogen evolution reaction, Electrochim. Acta 166 (2015) 26–31, https://doi.org/10.1016/j.electacta.2015.03.067.

[12] L. Xie, X. Ren, Q. Liu, G. Cui, R. Ge, A.M. Asiri, X. Sun, Q. Zhang, L. Chen, A Ni(OH) 2–PtO2 hybrid nanosheet array with ultralow Pt loading toward efficient and durable alkaline hydrogen evolution, J. Mater. Chem. 6 (5) (2018) 1967–1970, https://doi.org/10.1039/c7ta09990h.
[13] J. Deng, H. Li, J. Xiao, Y. Tu, D. Deng, H. Yang, H. Tian, J. Li, P. Ren, X. Bao, Triggering the electrocatalytic hydrogen evolution activity of the inert two-dimensional MoS_2 surface via single-atom metal doping, Energy Environ. Sci. 8 (5) (2015) 1594–1601, https://doi.org/10.1039/c5ee00751h.
[14] Y. Xin, S. Li, Y. Qian, W. Zhu, H. Yuan, P. Jiang, R. Guo, L. Wang, High-entropy alloys as a platform for catalysis: progress, challenges, and opportunities, ACS Catal. 10 (19) (2020) 11280–11306, https://doi.org/10.1021/acscatal.0c03617.
[15] H.-J. Qiu, G. Fang, J. Gao, Y. Wen, J. Lv, H. Li, G. Xie, X. Liu, S. Sun, Noble metal-free nanoporous high-entropy alloys as highly efficient electrocatalysts for oxygen evolution reaction, ACS Mater. Lett. 1 (5) (2019) 526–533, https://doi.org/10.1021/acsmaterialslett.9b00414.
[16] L. Wang, Y. Yang, J. Wang, W. Liu, Y. Liu, J. Gong, G. Liu, X. Wang, Z. Cheng, X. Zhang, Excellent catalytic performance toward the hydrogen evolution reaction in topological semimetals, EcoMat 5 (4) (2022), https://doi.org/10.1002/eom2.12316.
[17] L. Cai, J. Huo, P. Zou, G. Li, J. Liu, W. Xu, M. Gao, S. Zhang, J.Q. Wang, Key role of lorentz excitation in the electromagnetic-enhanced hydrogen evolution reaction, ACS Appl. Mater. Interfaces 14 (13) (2022) 15243–15249, https://doi.org/10.1021/acsami.2c00643.
[18] G. Li, Q. Yang, J. Rao, C. Fu, S.C. Liou, G. Auffermann, Y. Sun, C. Felser, In situ induction of strain in iron phosphide (FeP2) catalyst for enhanced hydroxide adsorption and water oxidation, Adv. Funct. Mater. 30 (12) (2020), 1907791, https://doi.org/10.1002/adfm.201907791.
[19] Y. Qiu, L. Xin, Y. Li, I.T. McCrum, F. Guo, T. Ma, Y. Ren, Q. Liu, L. Zhou, S. Gu, M. J. Janik, W. Li, BCC-phased PdCu alloy as a highly active electrocatalyst for hydrogen oxidation in alkaline electrolytes, J. Am. Chem. Soc. 140 (48) (2018) 16580–16588, https://doi.org/10.1021/jacs.8b08356.
[20] C. Wang, Y. Wang, H. Yang, Y. Zhang, H. Zhao, Q. Wang, Revealing the role of electrocatalyst crystal structure on oxygen evolution reaction with nickel as an example, Small 14 (40) (2018), 1802895, https://doi.org/10.1002/smll.201802895.
[21] Y.-R. Zheng, P. Wu, M.-R. Gao, X.-L. Zhang, F.-Y. Gao, H.-X. Ju, R. Wu, Q. Gao, R. You, W.-X. Huang, S.-J. Liu, S.-W. Hu, J. Zhu, Z. Li, S.-H. Yu, Doping-induced structural phase transition in cobalt diselenide enables enhanced hydrogen evolution catalysis, Nat. Commun. 9 (2533) (2018) 4954–4961, https://doi.org/10.1038/s41467-018-04954-7.
[22] J. Sun, J. Li, Z. Li, X. Hu, H. Bai, X. Meng, Phase transition in cobalt selenide with a greatly improved electrocatalytic activity in hydrogen evolution reactions, ACS Sustain. Chem. Eng. 10 (12) (2022) 4022–4030, https://doi.org/10.1021/acssuschemeng.2c00449.
[23] J. Bai, Y. Wang, Y. Wang, T. Zhang, G. Dong, D. Geng, D. Zhao, Temperature-induced structure transformation from Co0.85Se to orthorhombic phase CoSe2 realizing enhanced hydrogen evolution catalysis, ACS Omega 7 (18) (2022) 15901–15908, https://doi.org/10.1021/acsomega.2c01020.
[24] R. Xie, Z. Hou, G.L. Chai, Heusler alloy catalysts for electrochemical CO2 reduction, J. Chem. Phys. 157 (7) (2022), 074704, https://doi.org/10.1063/5.0100268.
[25] M. Yu, G. Li, C. Fu, E. Liu, K. Manna, E. Budiyanto, Q. Yang, C. Felser, H. Tuysuz, Tunable eg orbital occupancy in heusler compounds for oxygen evolution reaction, Angew Chem. Int. Ed. Engl. 60 (11) (2021) 5800–5805, https://doi.org/10.1002/anie.202013610.
[26] T. Kojima, S. Kameoka, A.P. Tsai, Heusler alloys: a group of novel catalysts, ACS Omega 2 (1) (2017) 147–153, https://doi.org/10.1021/acsomega.6b00299.
[27] T. Kojima, S. Kameoka, A.-P. Tsai, The emergence of Heusler alloy catalysts, Sci. Technol. Adv. Mater. 20 (1) (2019) 445–455, https://doi.org/10.1080/14686996.2019.1598238.
[28] S.K. Takayuki Kojima, Shinpei Fujii, Shigenori Ueda, An-Pang Tsai, Catalysis-tunable Heusler alloys in selective hydrogenation of alkynes: a new potential for old materials, Sci. Adv. 4 (2018) 6063, https://doi.org/10.1126/sciadv.aat606.
[29] G. Li, Q. Yang, K. Manna, Q. Mu, C. Fu, Y. Sun, C. Felser, Magnetocatalysis: the interplay between the magnetic field and electrocatalysis, CCS Chem. 3 (10) (2021) 2259–2267, https://doi.org/10.31635/ccschem.021.202100991.
[30] M.V. Lyange, E.S. Barmina, V.V. Khovaylo, Structural and magnetic properties of Ni-Mn-Al Heusler alloys: a review, Mater. Sci. 81–82 (2015) 232–242. http://www.ogp-cn.com/EN/10.4028/www.scientific.net/MSFo.81-82.232.
[31] T. Bachaga, J. Zhang, M. Khitouni, J.J. Sunol, NiMn-based Heusler magnetic shape memory alloys: a review, J. Adv. Manuf. Technol. 103 (5–8) (2019) 2761–2772, https://doi.org/10.1007/s00170-019-03534-3.
[32] Y. Feng, J.H. Sui, Z.Y. Gao, G.F. Dong, W. Cai, Microstructure, phase transitions and mechanical properties of Ni50Mn34In16−yCoy alloys, J. Alloys Compd. 476 (1–2) (2009) 935–939, https://doi.org/10.1016/j.jallcom.2008.09.149.
[33] X.Z. Li, W.Y. Zhang, S. Valloppilly, D.J. Sellmyer, New Heusler compounds in Ni-Mn-In and Ni-Mn-Sn alloys, Sci. Rep. 9 (1) (2019) 7762, https://doi.org/10.1038/s41598-019-44179-2.
[34] A. Deltell, L. Escoda, J. Saurina, J. Suñol, Martensitic transformation in Ni-Mn-Sn-Co Heusler alloys, Metals 5 (2) (2015) 695–705, https://doi.org/10.3390/met5020695.
[35] H. Zheng, W. Wang, J. Yu, Q. Zhai, Z. Luo, Martensitic transformation in melt-spun Heusler Ni–Mn–Sn–Co ribbons, J. Mater. Res. 29 (7) (2014) 880–886, https://doi.org/10.1557/jmr.2014.57.
[36] T. Krenke, X. Moya, S. Aksoy, M. Acet, P. Entel, L. Mañosa, A. Planes, Y. Elerman, A. Yücel, E.F. Wassermann, Electronic aspects of the martensitic transition in Ni–Mn based Heusler alloys, J. Magn. Magn Mater. 310 (2) (2007) 2788–2789, https://doi.org/10.1016/j.jmmm.2006.10.1139.
[37] A.T. Zayak, W.A. Adeagbo, P. Entel, K.M. Rabe, e/a dependence of the lattice instability of cubic Heusler alloys from first principles, Appl. Phys. Lett. 88 (11) (2006), 111903, https://doi.org/10.1063/1.2185046.
[38] B. Hernando, J.L. Sánchez Llamazares, V.M. Prida, D. Baldomir, D. Serantes, M. Ilyn, J. González, Magnetocaloric effect in preferentially textured Mn50Ni40In10 melt spun ribbons, Appl. Phys. Lett. 94 (22) (2009) 222502–222505, https://doi.org/10.1063/1.3147875.
[39] J.D. Santos, T. Sanchez, P. Alvarez, M.L. Sanchez, J.L. Sánchez Llamazares, B. Hernando, L. Escoda, J.J. Suñol, R. Varga, Microstructure and magnetic properties of Ni50Mn37Sn13 Heusler alloy ribbons, J. Appl. Phys. 103 (7) (2008), 07B326, https://doi.org/10.1063/1.2832330.
[40] B. Ingale, R. Gopalan, M. Rajasekhar, S. Ram, Studies on ordering temperature and martensite stabilization in Ni55Mn20−xGa25+x alloys, J. Alloys Compd. 475 (1–2) (2009) 276–280, https://doi.org/10.1016/j.jallcom.2008.08.004.
[41] C. Xing, H. Zhang, K. Long, Y. Xiao, H. Zhang, Z. Qiu, D. He, X. Liu, Y. Zhang, Y. Long, The effect of different atomic substitution at Mn site on magnetocaloric effect in Ni50Mn35Co2Sn13 alloy, Crystals 8 (8) (2018) 329–341, https://doi.org/10.3390/cryst8080329.
[42] J. Kibsgaard, T.F. Jaramillo, Molybdenum phosphosulfide: an active, acid-stable, earth-abundant catalyst for the hydrogen evolution reaction, Angew. Chem. Int. Ed. 53 (52) (2014) 14433–14437, https://doi.org/10.1002/anie.201408222.
[43] D. Voiry, M. Chhowalla, Y. Gogotsi, N.A. Kotov, Y. Li, R.M. Penner, R.E. Schaak, P. S. Weiss, Best practices for reporting electrocatalytic performance of nanomaterials, ACS Nano 12 (10) (2018) 9635–9638, https://doi.org/10.1021/acsnano.8b07700.
[44] L. Wu, J.P. Hofmann, Comparing the intrinsic HER activity of transition metal dichalcogenides: pitfalls and suggestions, ACS Energy Lett. 6 (7) (2021) 2619–2625, https://doi.org/10.1021/acsenergylett.1c00912.
[45] Y. Zhang, K.E. Arpino, Q. Yang, N. Kikugawa, D.A. Sokolov, C.W. Hicks, J. Liu, C. Felser, G. Li, Observation of a robust and active catalyst for hydrogen evolution under high current densities, Nat. Commun. 13 (1) (2022) 7784, https://doi.org/10.1038/s41467-022-35464-2.
[46] T. Shinagawa, A.T. Garcia-Esparza, K. Takanabe, Insight on Tafel slopes from a microkinetic analysis of aqueous electrocatalysis for energy conversion, Sci. Rep. 5 (2015), 13801, https://doi.org/10.1038/srep13801.
[47] R. Parsons, The rate of electrolytic hydrogen evolution and the heat of adsorption of hydrogen, Trans. Faraday Soc. 54 (1958) 1053–1063, https://doi.org/10.1039/tf9585401053.
[48] N.J. K, B. T, L. A, K.J. R, C.J. G, P. S, N.J. K, Trends in the exchange current for hydrogen evolution, J. Electrochem. Soc. 152 (3) (2005) 23–26, https://doi.org/10.1149/1.1856988.
[49] E. Santos, W. Schmickler, d-Band catalysis in electrochemistry, ChemPhysChem 7 (11) (2006) 2282–2285, https://doi.org/10.1002/cphc.200600441.
[50] E. Santos, A. Lundin, K. Pötting, P. Quaino, W. Schmickler, Model for the electrocatalysis of hydrogen evolution, Phys. Rev. B 79 (23) (2009) 235436–235446, https://doi.org/10.1103/PhysRevB.79.235436.
[51] H. Radinger, V. Trouillet, F. Bauer, F. Scheiba, Work function describes the electrocatalytic activity of graphite for vanadium oxidation, ACS Catal. 12 (10) (2022) 6007–6015, https://doi.org/10.1021/acscatal.2c00334.
[52] C. Beasley, M. Kumaran Gnanamani, E. Santillan-Jimenez, M. Martinelli, W. D. Shafer, S.D. Hopps, N. Wanninayake, D.Y. Kim, Effect of metal work function on hydrogen production from photocatalytic water splitting with MTiO 2 catalysts, ChemistrySelect 5 (3) (2020) 1013–1019, https://doi.org/10.1002/slct.201904151.
[53] Y. Luo, Y. Tang, T.F. Chung, C.L. Tai, C.Y. Chen, J.R. Yang, D.Y. Li, Electron work function: an indicative parameter towards a novel material design methodology, Sci. Rep. 11 (1) (2021), 11565, https://doi.org/10.1038/s41598-021-90715-4.
[54] S. Trasatti, Work function, electronegativity, and electrochemical behaviour of metals: III. Electrolytic hydrogen evolution in acid solutions, J. Electroanal. Chem. Interfacial Electrochem. 39 (1) (1972) 163–184, https://doi.org/10.1016/S0022-0728(72)80485.
[55] Y. Li, P. Zhang, D. Wan, C. Xue, J. Zhao, G. Shao, Direct evidence of 2D/1D heterojunction enhancement on photocatalytic activity through assembling MoS2 nanosheets onto super-long TiO2 nanofibers, Appl. Surf. Sci. 504 (2020), https://doi.org/10.1016/j.apsusc.2019.144361.
[56] Y. Wang, W. Qiu, E. Song, F. Gu, Z. Zheng, X. Zhao, Y. Zhao, J. Liu, W. Zhang, Adsorption-energy-based activity descriptors for electrocatalysts in energy storage applications, Natl. Sci. Rev. 5 (3) (2018) 327–341, https://doi.org/10.1093/nsr/nwx119.
[57] Berit Hinnemann, Poul Georg Moses, Jacob Bonde, Kristina P. Jørgensen, Jane H. Nielsen, Sebastian Horch, Ib Chorkendorff, Jens K. Nørskov, Biomimetic hydrogen evolution: MoS2 nanoparticles as catalyst for hydrogen evolution, J. Am. Chem. Soc. 15 (2005) 5308–5309, https://doi.org/10.1021/ja0504690.
[58] P. Searson, P. Nagarkar, R. Laianision, The effect of density of states, work function and exchange integral of olycrystalline and single crystal surfaces on the hydrogen evolution reaction, Hydrogen Energy 14 (2) (1989) 131–136, https://doi.org/10.1016/0360-3199(89)90002-5.

[59] Oleg A. Petrii, Galina A. Tsirlina, Electrocatalytic activity prediction for hydrogen electrode reactions: intuition, art, science, Electroehimico. Acta 39 (11) (1993) 1739–1747, https://doi.org/10.1016/0013-4686(94)85159-X.
[60] J.K. Nørskov, F. Abild-Pedersen, F. Studt, T. Bligaard, Density functional theory in surface chemistry and catalysis, Proc. Natl. Acad. Sci. USA 108 (3) (2011) 937–943, https://doi.org/10.1073/pnas.1006652108.
[61] L. Yu, Q. Yan, A. Ruzsinszky, The key role of antibonding electron transfer in surface chemisorption and heterogeneous catalysis, Phys. Rev. Mater. 3 (2019) 2801–2822, https://doi.org/10.1103/PhysRevMaterials.3.092801.